Article

Impact of Assimilating FORMOSAT-7/COSMIC-2 Radio Occultation Data on Typhoon Prediction Using a Regional Model

Ying-Jhen Chen, Jing-Shan Hong * and Wen-Jou Chen

Central Weather Bureau, No. 64, Gongyuan Road, Taipei 100006, Taiwan
* Correspondence: rfs14@cwb.gov.tw

Abstract: As the successor of FORMOSAT-3/COSMIC (FS3/C1), FORMOSAT-7/COSMIC-2 (FS7/C2) was successfully launched on 25 June 2019. FS3 radio occultation (RO) data has contributed greatly to Taiwan's meteorological progress, improving model representations of marine boundary layer heights, cyclogenesis, tropical cyclones/typhoons, and Mei-Yu front systems. The operational CWBWRF numerical weather prediction model with the 3DEnVar data assimilating system in the Taiwan Central Weather Bureau (CWB) was adopted to evaluate the impact of assimilating FS7 RO data. The following two experiments were conducted: one assimilated the in-situ observations as in the CWB operational task (nRO), and the other additionally assimilated FS7 RO refractivity profiles (wRO). Both experiments utilized 6-h assimilating window and full cycle data assimilation strategy and made 120-h forecasts after each assimilation. Within over 70 synoptic verification cases, the biases of geopotential height, temperature, and wind were reduced in the upper model levels in wRO results, and the typhoon track and intensity prediction error reductions were statistically significant. In addition, the wRO experiment improved the typhoon structure in the initial conditions and led to a better typhoon structure forecast. These results showed that the FS7 RO refractivity assimilation could improve model forecast performance, leading to its operational use in the CWB.

Keywords: FORMOSAT-7/COSMIC-2; radio occultation (RO); typhoon; hybrid WRFDA

1. Introduction

Taiwan is located in the western Pacific Ocean and is frequently affected by typhoons, with an average of three to four tropical cyclones (TC)/typhoons landfalls every year. For disaster risk mitigation and preemptive hazard response, Taiwan highly depends on reliable and timely typhoon forecast guidance. Good forecast guidance relies on the robust numerical weather prediction (NWP) system. Particularly, the initial condition plays an important role in model forecast performance. The state-of-the-art data assimilation system provides an improved estimate of the atmospheric state, by which observations are combined with a model's first guess or background forecast and their respective error statistics.

However, observations are distributed unevenly due to orography. Over land, abundant synoptic stations, and various high-frequency measurements, such as radars and wind profilers, can provide automatic periodic observations. On the contrary, over the ocean, there are only a few conventional observation types, such as radiosondes, aircraft, and buoys. Therefore, sampling over oceans highly depends on satellite observations, which are not limited by orography.

To overcome observation deficiencies, especially over the oceans, Taiwan and the United States cooperated on the Formosa Satellite Mission 3 (FORMOSAT-3, hereafter FS3) Constellation Observing System for Meteorology, Ionosphere, and Climate (COSMIC [1]) mission and launched six microsatellites on 15 April 2006. With the Global Navigation Satellite System (GNSS) radio occultation (RO) technique [2,3], FS3 can receive signals from Global Positioning System (GPS) satellites and retrieve vertically resolved atmospheric

profiles in the ionosphere and lower atmosphere. FS3 has provided more than 6 million RO profiles over the past 14 years before it was decommissioned on 1 May 2020.

Besides the FS3, many satellites employ the GNSS RO technique, such as Challenging Minisatellite Payload (CHAMP [4,5]), Satélite de Aplicaciones Científicas-C (SAC-C [6]), Gravity Recovery and Climate Experiment (GRACE [7]), Meteorological Operational satellite series (MetOp-A/B/C [8]), and Korea Multi-Purpose Satellite-5 (KOMPSAT-5 [9]). In recent years, RO data has been essential in major operational NWP centers, such as the European Center for Medium-Range Weather Forecasts (ECMWF), the National Centers for Environmental Prediction (NCEP), the UK Met Office, and Meteo France. The operational NWP in Taiwan's Central Weather Bureau (CWB) is no exception [10].

Compared with other measurement techniques, RO data can continuously provide highly accurate and precise atmospheric profiles, with vertical resolutions as high as a few hundred meters. Cloud cover and precipitation usually affect infrared and microwave-based satellites but not RO observations. Therefore, RO data do not need extra calibration or bias correction [11]. With supplemental data from other observations or global analysis, RO data can be used to retrieve atmospheric temperature and moisture information [12].

FS3 RO data was applied in various fields such as weather, climate, and space weather and has made significant contributions to the scientific community (Ho et al. (2020) [13]). For Taiwan's NWP progress, the implementation of FS3 RO data has been shown to greatly contribute to a wide variety of important issues, such as improving model representations of marine boundary layer heights [14,15], cyclogenesis [16,17], TCs [10,18–23], and Mei-Yu front systems [24–26].

Due to the widespread deployment of FS3 RO data and its remarkable performance, Taiwan and the United States continued with the follow-on mission, the Formosa Satellite Mission 7 (FORMOSAT-7, hereafter FS7)/COSMIC-2 program. FS7 integrates six constellation satellites equipped with the Tri-GNSS RO System (TGRS), which can receive signals from both the GPS and the Russian Globalnaya Navigatsionnaya Sputnikovaya Sistema (GLONASS). The flight altitude of FS7 is 550 km with an inclination angle of $24°$. FS7 can provide at least 4000 RO soundings per day over the tropics and subtropics region from $45°N$ to $45°S$, and this number is more than twice that of FS3. With a higher signal-to-noise ratio (SNR) antenna, FS7 can receive rays with deeper penetration into the troposphere and obtain more information about atmospheric boundary layer and super-refraction (SR) characteristics. FS7 satellites were successfully launched on 25 June 2019, and completed orbit transfer in the first season of 2021. FS7 RO sounding data can be freely accessed from two processing centers, namely, the COSMIC Data Analysis and Archive Center and the Taiwan Analysis Center for COSMIC (TACC).

After FS7 was launched, the data quality was verified by comparing it with other independent data, such as radiosondes, model forecasts, and reanalyses [27–38]. As the first summary of the initial FS7 quality assessment, Schreiner et al. (2020) [27] confirmed that FS7 RO data meet expectations of high accuracy and precision. They also pointed out that FS7s higher SNR would enable deeper tropospheric penetration, improving the observation of atmospheric boundary height and SR detection.

Ho et al. (2020) [30] validated FS7 RO data with Vaisala RS41 radiosonde observations. They also assessed the FS7 data quality in terms of stability, precision, and accuracy. In their results, the uncertainty of FS7 accuracy is very compatible with those from FS3, and the higher SNR seemed to improve the mean FS7-RS41 water vapor difference from the surface to 5 km altitude. Chen et al. (2020) [31] showed that 80% of FS7 RO profiles could penetrate deeper than 1 km. They also compared FS7 RO data retrievals with different kinds of observations, including dropsondes, radiosondes, RO data retrievals from different satellite missions, global analyses, and satellite retrievals from the NOAA Unique Combined Atmospheric Processing System. The comparisons demonstrate that the RO wet retrievals (i.e., wetPf2) showed small deviations (less than 0.5 $°C$) in FS7 temperature in the troposphere and around ±2 hPa in vapor pressure with other observations.

Anthes et al. (2021) [34] computed the biases and standard deviations of differences in FS7 temperature, specific humidity, and precipitable water with respect to four reanalyses of Hurricane Dorian (2019). They also estimated the random error standard deviations of all four datasets using the three-cornered hat method. The error statistics showed that FS7 RO data were not obviously degraded by the clouds and precipitation in the hurricane and its environment.

Through the data assimilation (DA) technique, the precise and accurate information from FS7 RO data can be used to correct the model errors and obtain a better model initial condition. Ruston and Healy (2020) [28] assessed the impact of FS7 bending angle assimilation on the short-range forecast with four-dimensional variational assimilation (4DVar). Their results indicated that FS7 measurements had a clear impact on upper tropospheric and stratospheric temperatures and winds, as expected. A novel finding is the improvement of tropical tropospheric humidity forecasts, which had been difficult to demonstrate prior to FS7.

Singh et al. [35] evaluated the impact of assimilating FS7 RO refractivity profiles on the Weather Research and Forecasting (WRF) model short-range forecasts over the Indian region. The WRF model employed the three-dimensional variational assimilation (3DVar) system, and the experiment period was during the summer monsoon season (June to September 2020). With FS7 RO data, the precipitation prediction skill improved by 20%, and the forecast/analysis errors were reduced by 8–10%. They also pointed out that the default quality control (QC) procedure employed in the 3DVar was too conservative to retain the positive impact in the lower troposphere.

Numerous studies have focused on the effect of FS7 data on modeling high-impact weather systems in the vicinity of Taiwan. Chen et al. [36] demonstrated that assimilating FS7 RO refractivity with WRF 3DVar can bring a neutral to a slightly positive impact on the Mei-Yu moisture indicator for daily monitoring in the South China Sea and the Bay of Bengal. The forecast samples with RO DA simulated a better structure and intensity of Typhoon Hagupit (2020), and the data effect could be amplified via repeated RO DA cycles. Chen et al. [37] first compared the impacts of local and nonlocal operators to assimilate RO refractivity data in a WRF 3DEnVar Hybrid System (combining 3DVar and an ensemble transform Kalman filter). The RO data with a nonlocal operator contributes to a remarkable improvement in typhoon track prediction through Typhoon Hagupit's (2020) and Haishen's (2020) case studies. Chang and Yang (2022) [38] also assimilated FS7 refractivity but used the WRF local ensemble transform Kalman filter (WRF-LETKF) hybrid DA system. As expected, assimilating with FS7 RO data would improve low-level moisture analysis; however, they found that excluding the RO data below 3 km facilitated better rainfall prediction. The sensitivity experiments also revealed that the RO QC procedure is more influential than observation error variance adjustment on rainfall prediction especially utilizing low-level RO data.

The Taiwan CWB also evaluated the FS7 provisional data for assimilating impact within the operational model. Lien et al. [29] conducted a parallel semi-operational experiment assimilating the FS7 bending angle data and all operational observation data within the CWB Global Forecast System (CWBGFS) [39]. Their results showed that the FS7 RO data made a significant positive forecast impact in the tropical region. Their sensitivity experiments of the QC procedures built into the Gridpoint Statistical Interpolation (GSI) system indicated that the QC processes worked well, while the observation error should be tuned further. Their results also implied the importance of FS7 RO data and facilitated its operational usage in CWBGFS since 15 September 2020.

The operational regional NWP system, named CWBWRF, is responsible for providing high-resolution short-term (5 days long) deterministic forecasts in CWB. The domain of CWBWRF overlays with FS7 data coverage. This study aims to assess the impact of FS7 RO data on the CWBWRF hybrid DA system from the synoptic verification and typhoon track forecast. This paper is organized as follows: Section 2 describes the experiment settings, including the CWBWRF model configuration and the DA strategy, the QC procedures used

in CWBWRF, and the experiment design. Section 3 presents the FS7 RO DA statistics in QC rejection rate, innovations and increments characteristics, and synoptic verifications. Section 4 focuses on the FS7 RO data impacts on typhoon forecasts in the experiment period and a complement case study of Typhoon Hagibis (2019). Finally, the conclusion is presented in Section 5.

2. Experiment Settings

2.1. CWBWRF Model Configuration and DA Strategy

The operational NWP deterministic system, CWBWRF, was constructed in November 2007 based on the Advanced Research WRF (WRF-ARW) model (Skamarock et al., 2008 [40]). The CWBWRF has two nested domains centered on Taiwan. The resolution of the outer domain is 15 km with 662×386 grid points (Figure 1), and the inner domain is 3 km with 1161×676 grid points. The model has 52 vertical levels from the surface to 20 hPa. The physics parameterization schemes include the Yonsei University PBL Scheme [41], the Goddard microphysics scheme [42], the RRTMG shortwave and longwave schemes [43], and the Noah land surface model [44].
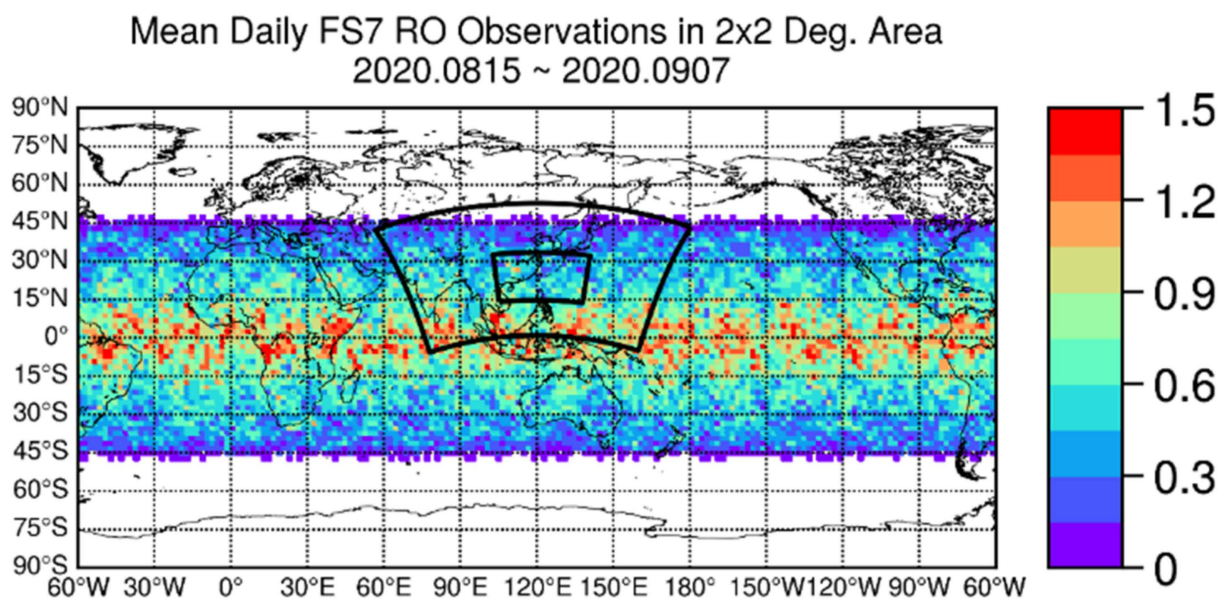

Figure 1. Number of mean daily FS7 RO profiles in 2×2 degrees areas from 15 August to 7 September 2020. The black frames show the CWBWRF 15-km (outer) and 3-km (inner) domain coverage, but the 3-km domain is not used in this paper.

To obtain a better and more reliable initial condition, CWBWRF adapted the WRF data assimilation system (WRFDA). The DA method is a hybrid 3DEnVar whose background error covariance (BEC) is composed of 75% flow-dependent characteristics provided by the ensemble adjustment Kalman filter system and 25% static statistics from the 3DVar technique with the "CV5" option in WRFDA. This option means that the static BEC uses five control variables, including stream function, unbalanced velocity potential, unbalanced surface pressure, unbalanced temperature, and pseudo relative humidity. Operationally, CWBWRF runs four times a day. A so-called partial cycle strategy, conducted with a cold start analysis from the NCEP Global Forecast System (GFS) at the previous 12 h and cycling twice in every 6 h interval, is applied to provide the model's initial condition. This strategy takes advantage of the GFS analysis to appropriately handle the large-scale environment at the previous 12 h and reduce the model spin-up from the cyclic mesoscale DA. The lateral boundary conditions are taken from the NCEP GFS real-time forecasts at 6-h intervals. The data assimilated in CWBWRF operationally include synoptic observations,

ship observations, meteorological terminal aviation weather reports, soundings, airplane reports, buoys, satellite soundings, and ground-based GPS zenith total delay data.

2.2. FS7 RO Data

With more assumptions and processing, the retrieved higher-level RO products can provide more meteorological information and the corresponding forward observation operator is easier to construct. However, this also means that there would be extra errors induced during the retrieval process. FS7 RO can provide many kinds of retrieval data, such as excess phase, bending angle, refractivity, temperature, and moisture. Each kind of RO data has its own advantages and limitations. Most research and operational NWP systems choose to assimilate either bending angle or refractivity [10,16,24,25,28,29,32,33,45–48]. In this study, the refractivity profiles from the level 2 FS7 RO atmPrf data were assimilated. The FS7 atmPrf product contains full-resolution profiles with vertical spacing on the order of ten meters. Due to the high SNR antenna, most of the profile data can be retrieved below 1 km relative to the mean sea level [31] and is expected to benefit the high-resolution DA.

Figure 1 shows the mean daily FS7 RO profile distribution globally in $2° \times 2°$ grid boxes from 15 August to 07 September 2020. In most of the tropical regions (between $\pm15°$ latitudes), the six FS7 satellites can provide at least one profile per day, and the data amount decreases with increasing latitude from the equator to 45° N/S. FS7 RO data are distributed densely and evenly from the subtropics to the tropics, implying that FS7 RO could possibly eliminate data deficiency problems, especially over the ocean region.

In the WRFDA system, RO data has its own preprocessing, including QC and data thinning, which are both carried out prior to assimilation. There are four RO QC procedures in CWB WRFDA, namely, (1) a gross error check; (2) percent error control; (3) a vertical gradient of refractivity check; (4) an NCEP-GSI regional innovation check.

1. In the gross error check, the data is rejected when the absolute value of innovation, i.e., the difference between the observed value (O) and the model background value (B), is greater than five times of the observation error. The factor of five is the value suggested by the National Center for Atmospheric Research. This method is generally used in DA systems to avoid assimilations of observations with large biases from the model background;

2. Percent error control is a similar threshold to the innovation relationship. In percent error control, the data is rejected when the ratio of innovation (O-B) to the average between observation and model background is larger than a specific threshold, then. The thresholds are 0.05% below 7 km, 0.04% between 7 and 25 km, and 0.10% above 25 km [45];

3. The vertical gradient of refractivity was further checked. When the derivative of either observational or model refractivity with respect to height is less than -50 km^{-1} or the second derivative of refractivity with respect to height is greater than 100 km^{-2} then the data is rejected [49]. The first and second derivatives of refractivity represent the gradient and curvature of the ray path, respectively. Large vertical refractive gradients or curvatures occur when rays with tangent points inside the layer are trapped in the duct. This condition is known as SR, or ducting. Assimilating the GPS RO data with SR layers causes an ill-conditioned problem; thus, the observations need to be rejected in the assimilation algorithms [50];

4. The NCEP-GSI regional innovation check is the last step. Here, the data is rejected when the absolute value of innovation (O-B) is greater than or equal to the product of the standard deviation and the cutoff value. This QC criterion was modified from the NCEP GSI global DA in Cucurull et al. (2010) [51] for regional DA. The thresholds consider the data location (latitude), geometric height, and temperature of the RO profile at the same time.

Since FS7 RO data has a high vertical data density relative to the model's vertical resolution, after QC procedures, only observations nearest to the model layer would be ingested through data thinning to avoid overfitting.

2.3. Experiment Period

The impact of assimilating FS7 RO data on CWBWRF is the issue of interest in this study. Moreover, this study focuses on the RO impact on the 15 km resolution (the domain coverage is shown with the larger black frame in Figure 1), and two experiments were conducted. Both experiments assimilated conventional in-situ observations as in the operational configuration. The only difference was whether we assimilate FS7 RO refractive profiles or not, and these experiments are referred to as wRO and nRO, respectively. The DA frequency was four times per day on 00/06/12/18 UTC, and the assimilating window was set to be ±3 h. This study applied a full cycling strategy to enhance the accumulated effect of the RO impact, which means that the first guess is a 6-h forecast from the previous cycle. The experimental period is made every 6 h from 1200 UTC 15 August to 1200 UTC 07 September 2020. The cold start was conducted using NCEP GFS analysis of 0.5° × 0.5° resolution at 1200 UTC 15 August 2020. In this period, both experiments (wRO and nRO) accumulated 93 forecast cases, each with a 120-h forecast length. It should be noted that there were three typhoons, namely, Bavi, Maysak, and Haishen, with lifetimes of more than 5 days in the domain during this period.

Figure 2 shows the counts of assimilated FS7 RO profiles in the model domain within ±3-h DA windows during the experiment periods. As shown in the figure, the numbers of the FS7 RO profiles have an average of 400–600 per day during the experimental period. Although the orbit transfer of FS7 had not yet reached its final status during this period, the data counts seemed stable in every DA cycle.
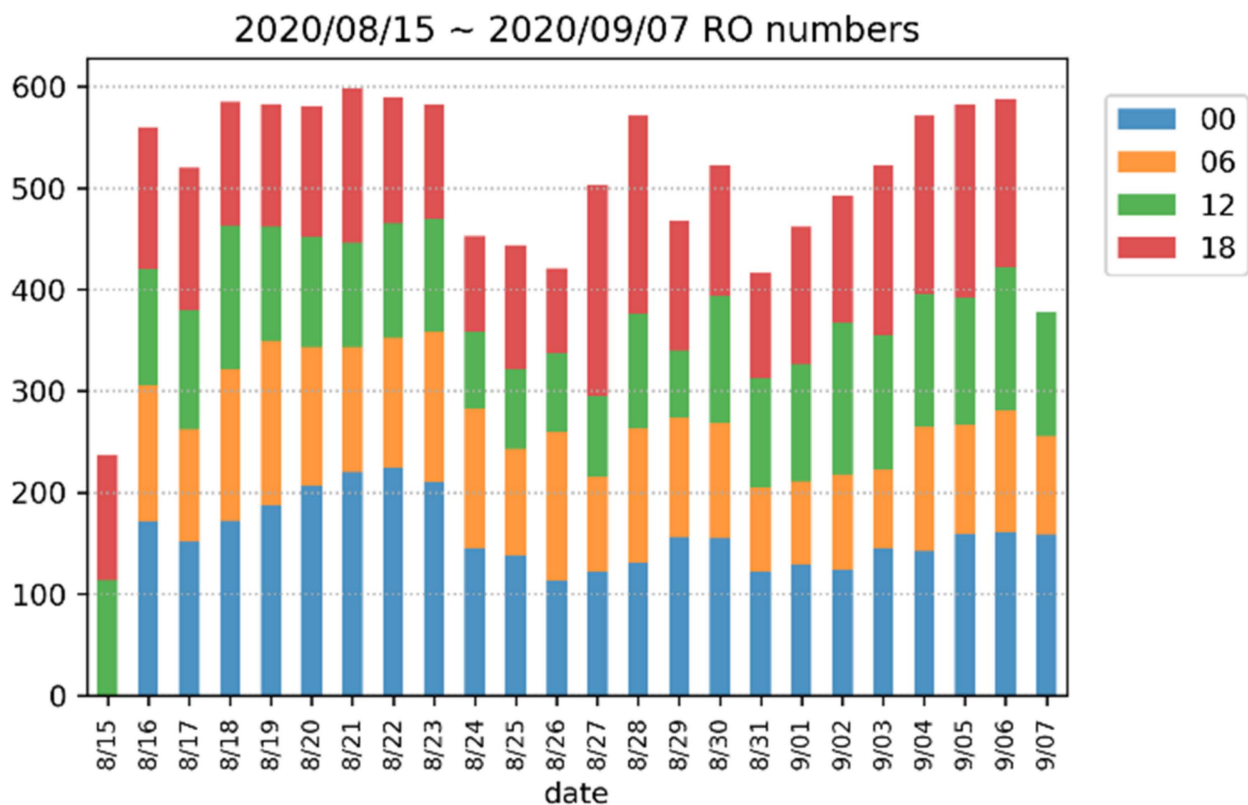

Figure 2. FS7 RO profile counts in CWBWRF domain within ±3-h data assimilation window for 00/06/12/18 UTC from 1200 UTC 15 August to 1200 UTC 7 September 2020.

3. Results

3.1. QC Rejection Rate

The forecast near the model top is generally contaminated due to the numerical treatment of the upper boundary conditions. Therefore, only the refractivity profile data below 18 km were assimilated (the altitudes mentioned in this study are geometric heights

unless otherwise noted). Figure 3a shows the FS7 RO counts in the experiment domain before QC (blue line) and after QC (orange line) during the experiment period. Statistics were binned in 1-km height bins. The original FS7 RO profiles have a high vertical data density (the data spacing is as fine as a few ten meters), and the counts decrease from around 6 million to 2.5 million as height descends from 16 km to near the surface. After QC, the counts decreased rapidly, especially under 8 km. Figure 3b shows the percentage of data rejected by QC. High rejection rates appear below 6 km and continue to increase as height decreases. Under 1 km, the data passing QC were rare (less than 5%), suggesting that although the FS7 signal can penetrate down to near the surface, the data might be eliminated in the end due to the QC criteria. To mitigate this situation, either decreasing the observation error of FS7RO data or relaxing the QC criteria could be attempted. Chang and Yang (2022) [38] addressed these issues in a heavy rainfall case. In their results, adjusting the QC procedure for rainfall prediction was more crucial than the observation error variance adjustment. To optimize the impact of low-level RO data, they emphasized that a sophisticated QC procedure should be developed.
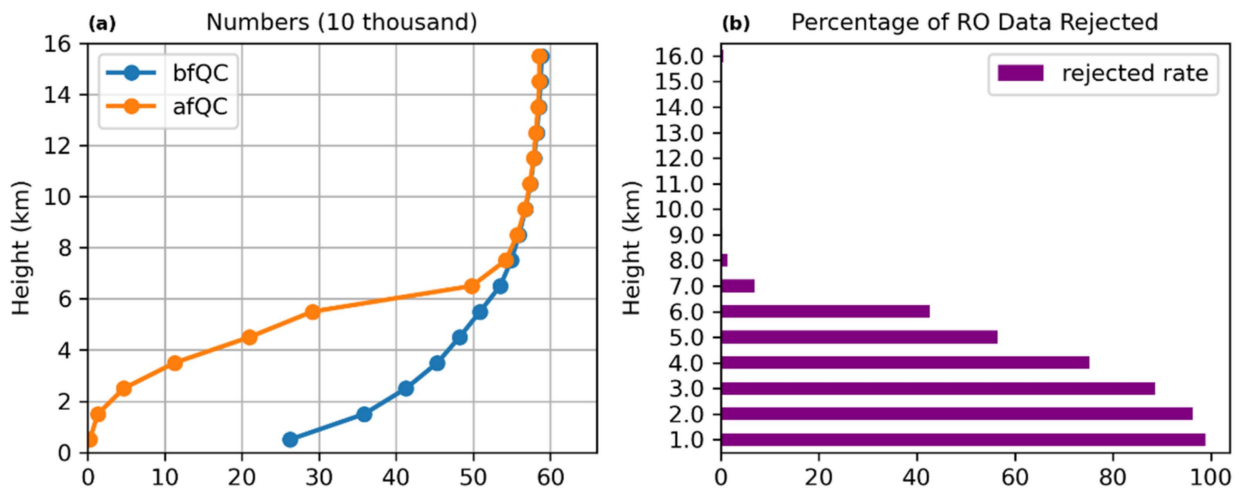

Figure 3. (**a**) Statistics of the F7/C2 RO counts in the experiment domain before QC (blue line) and after QC (orange line) during the experimental period. (**b**) Rejection rates.

3.2. Innovation Statistics

The statistics of observation minus background (OmB) and observation minus analysis (OmA) of the FS7 RO refractivity data in the wRO experiment are shown in Figure 4. The mean error (ME) and root mean square error (RMSE) were normalized by the observations. The statistics of OmB and OmA in the experiment period were calculated as follows:

$$\text{OmB\_ME} = \frac{1}{n} \sum_{i=1}^{n} \left(\frac{O_i - B_i}{O_i} \right) \times 100 \tag{1}$$

$$\text{OmA\_ME} = \frac{1}{n} \sum_{i=1}^{n} \left(\frac{O_i - A_i}{O_i} \right) \times 100 \tag{2}$$

$$\text{OmB\_RMSE} = \sqrt{\frac{1}{n} \sum_{i=1}^{n} \left[\left(\frac{O_i - B_i}{O_i} \right) \times 100 \right]^2} \tag{3}$$

$$\text{OmA\_RMSE} = \sqrt{\frac{1}{n} \sum_{i=1}^{n} \left[\left(\frac{O_i - A_i}{O_i} \right) \times 100 \right]^2} \tag{4}$$

where n is the total data counts in every 1-km bin height. O_i, B_i, and A_i are the observation, model background, and model analysis values of the ith refractivity (N) data, respectively. In Figure 4, the ME of OmB, also called "innovation", shows a positive bias between 3 and 10 km, decreases below 3 km, and has an obviously negative bias especially under 1 km prior to the QC procedure. After RO data preprocessing, the negative bias was eliminated, and the positive bias under 4 km height was mitigated. The RO QC also had a strong impact on RMSE. Below 8 km, all RMSE values before QC were greater than 1%, even approaching 5% when the data was closer to the surface. After QC, the RMSE was reduced, especially under 4 km. This feature was caused by the NCEP-GSI regional innovation check, as mentioned in Section 2.2, since the stricter QC criteria were being applied in this step, especially for the data located under 4 km. As shown by the data rejection rate in Figure 3b, only a smaller percentage of data passes RO preprocessing under 4 km. However, after QC, the remaining data can improve both the RMSE and ME of the OmA compared to the OmB.
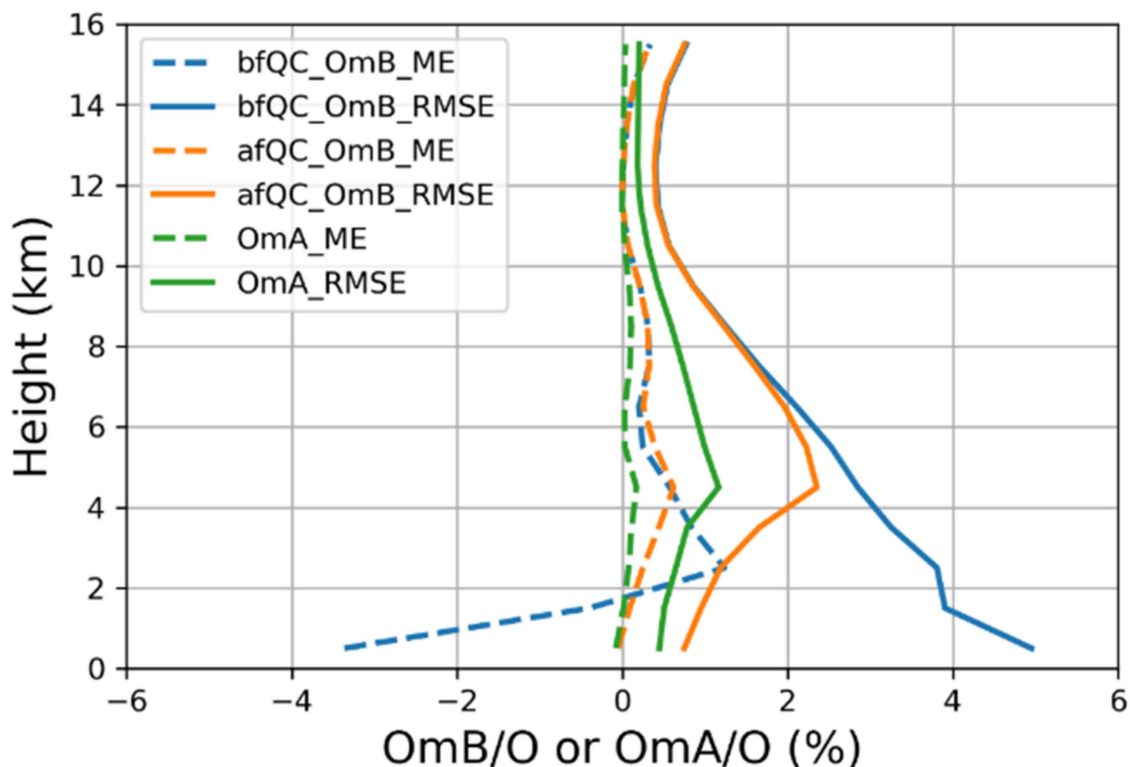

Figure 4. Observation minus background (OmB) and observation minus analysis (OmA) statistics for the FS7 RO refractivity data in wRO experiment. Mean error (ME; dashed lines) and root mean square error (RMSE; lines) of OmB before QC (blue line), OmB after QC (orange line), and OmA after QC (green line) with respect to height (km). The period is the same as that in Figure 2.

3.3. Assimilation Impact of the RO Observations

To assess the impact of assimilating FS7 RO data, this study first calculates the analysis increments, defined as the model analysis minus background, of every case. By subtracting the increments of nRO from those of wRO experiments, the impact of the assimilation of the RO observations on the analysis was obtained. Figure 5 shows the mean increment differences during the whole experiment period from 1200 UTC 15 August to 1200 UTC 7 September 2020. As shown in Figure 5a–c, the impact of the assimilation of the RO observations statistically drops the temperature over the center of the domain at 500 and 300 hPa and increases the temperature at 850 hPa. In addition, the RO impact increases the moisture throughout the whole atmosphere, as shown in Figure 5d–f.
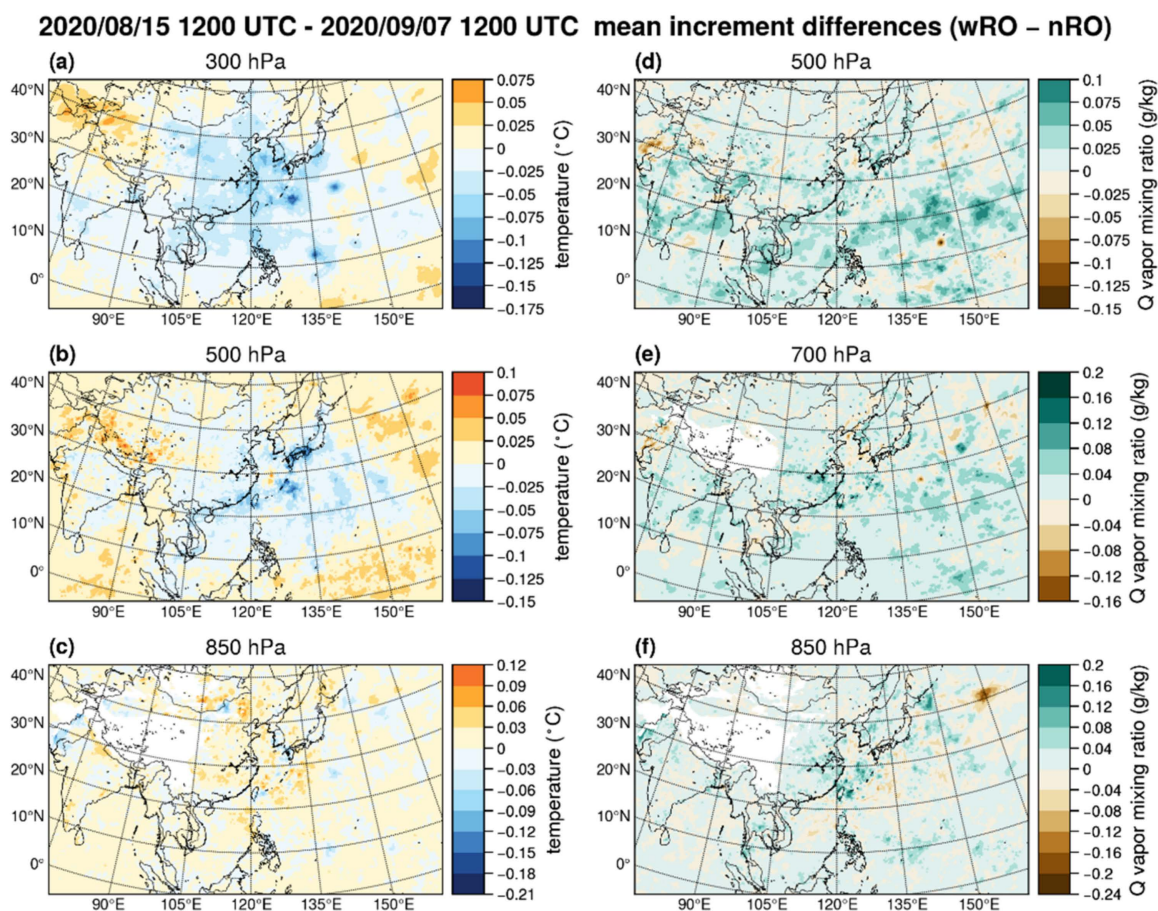
Figure 5. Mean differences of analysis increments between wRO and nRO experiments. The statistic period is the same as that in Figure 2. The mean temperature analysis increment is shown at the left column: (**a**) 300, (**b**) 500, and (**c**) 850 hPa height. The mean water vapor mixing ratio analysis increment is shown at the right column: (**d**) 500, (**e**) 700, and (**f**) 850 hPa. Positive (negative) value indicates that wRO experiment usually has larger (smaller) mean increment than nRO.

3.4. Synoptic Verifications

To understand the effect of FS7 RO refractivity assimilation on the model forecast, the experiment forecasts against the NCEP GFS analysis of 0.25° × 0.25° (i.e., nRO or wRO minus NCEP GFS) were compared, and ME and RMSE at 0, 72, and 120 forecast hours, respectively, were computed. Figure 6 shows the vertical profiles of ME and RMSE for geopotential height (H), temperature (T), relative humidity (RH), and u, v wind speed (U and V), the RMSE differences (i.e., wROs minus nROs at each level) with 95% confident intervals (CI), and the RMSE reduction ratios, which were calculated by the RMSE differences between nRO and wRO and averaged over all heights. Compared with nRO, wRO has smaller absolute ME and RMSE values at most levels. The fact that MEs of wRO are closer to the 0 value shows that FS7 RO refractivity assimilation could reduce the model forecast bias, for instance, for temperatures above 500 hPa and RH above 700 hPa. The maximum improvement occurs in the upper-level geopotential height, temperature, and winds, as shown in the RMSEs (Figure 6b,f,j,n,r). The most impressive improvement in RH is in the middle troposphere between 750 and 250 hPa in Figure 6j. These results are comparable to Singh et al. (2021) [35]. The RMSE improved by assimilating FS7 RO, especially at 0 and 72 forecast hours, as demonstrated within 95% CI (Figure 6c,g,k,o,s). As shown in Figure 6d,h,l,p,t, although the model forecast errors grow with the forecast length, the RMSE reduction ratios show that FS7 RO refractivity assimilation can improve forecast ability effectively even until 120 h.
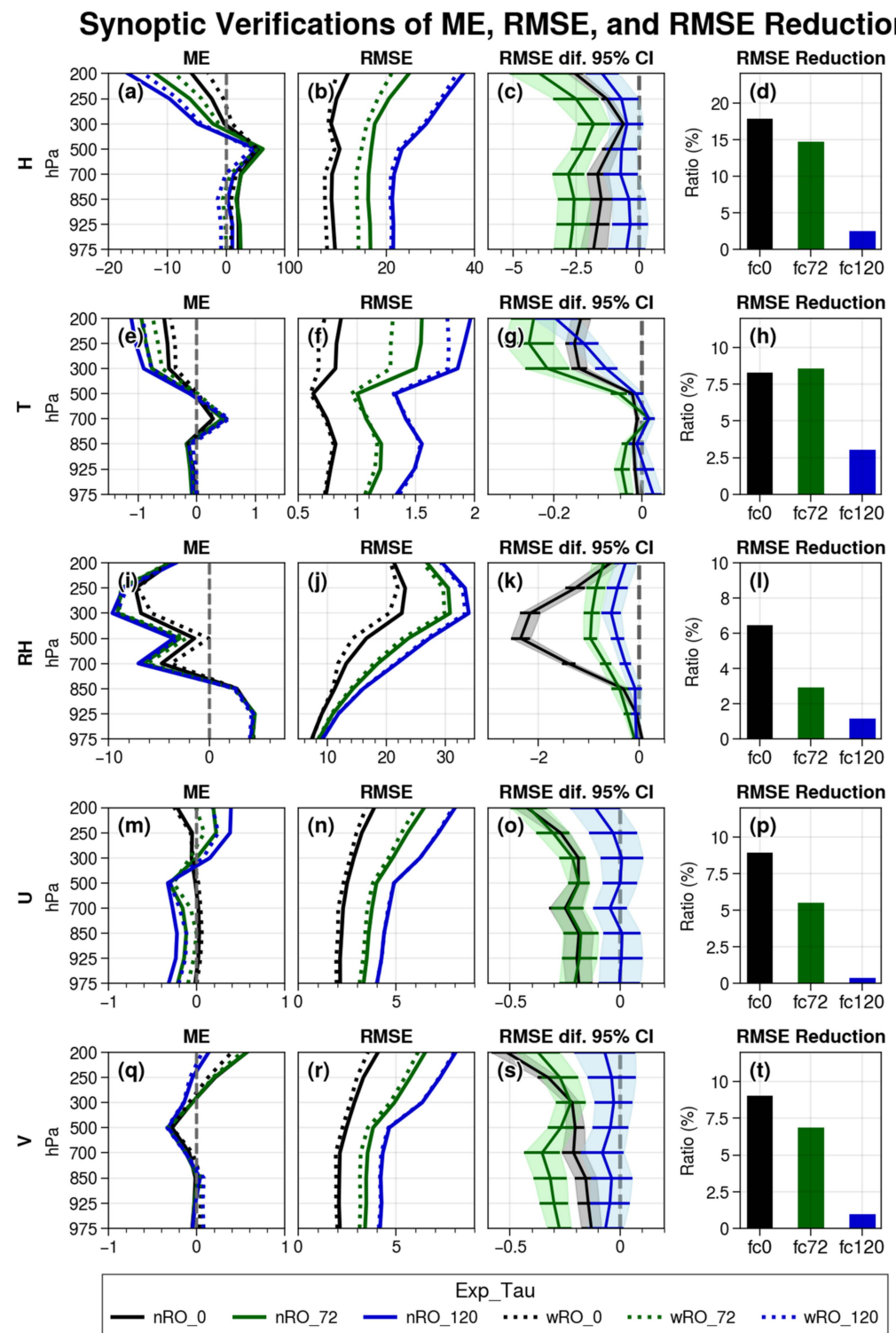
Synoptic Verifications of ME, RMSE, and RMSE Reduction

Figure 6. Grid verifications of nRO and wRO forecasts against the 0.25° × 0.25° NCEP GFS analysis. Averaging with a total of 93 cases (the same period as in Figure 2), (**a,e,i,m,q**) the vertical profiles of ME (the first column), (**b,f,j,n,r**) RMSE (the second column), (**c,g,k,o,s**) RMSE differences with 95% confident interval (CI) (the third column), and (**d,h,l,p,t**) RMSE reduction ratio (the fourth column) are computed at 0 (black), 72 (green), and 120 (blue) forecast hours, and presents in geopotential height (H, unit: meter), temperature (T, unit: K), relative humidity (RH, unit: %), and u and v wind speed (U and V, unit: m/s), respectively. The RMSE reductions were computed by the RMSEs of (nRO − wRO)/nRO × 100%.

Following previous results, the variations of ME and RMSE between nRO and wRO were investigated further during the experiment period. Figures 7 and 8 show the domain-averaged ME and RMSE vertical profile differences (i.e., wRO − nRO), respectively, for the 72-h forecasts as a function of the 93 initial times. These are the same as the results (green dashed line minus solid line) in Figure 6, but without time averaging. Compared with the domain-averaged ME shown in Figure 6, FS7 RO refractivity assimilation can mitigate model bias over most levels effectively. Examples are the cold bias above 300 hPa (Figure 7b), the dry bias above 700 hPa (Figure 7c), and the overly strong wind under 700 hPa (Figure 7d,e).
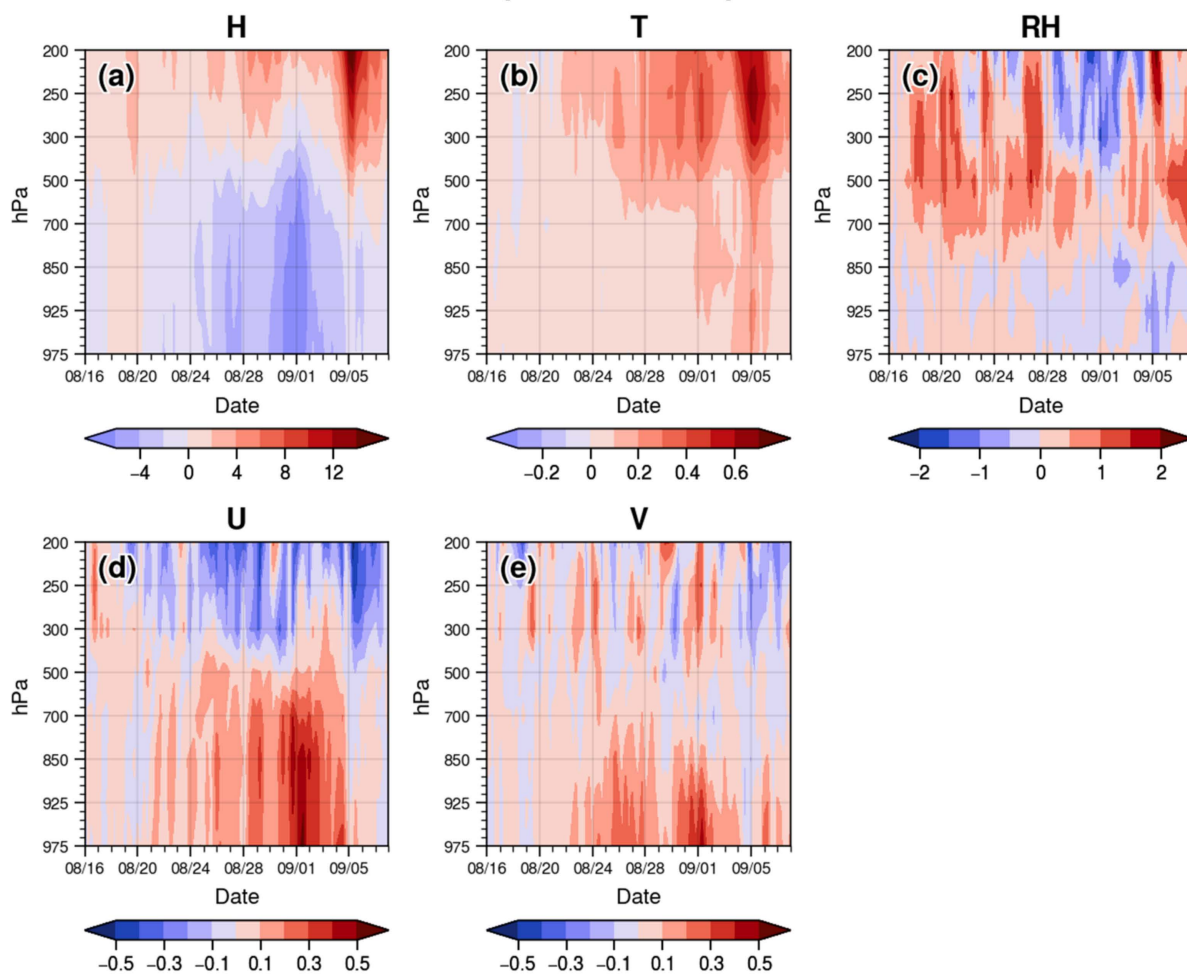
ME Difference (wRO−nRO) at 72 h Forecast

Figure 7. ME difference of 72-h forecast grid verification between nRO and wRO against 0.25° × 0.25° NCEP GFS analysis. The vertical profiles vary with the 93 initial time during the experiment period in (**a**) geopotential height (H, unit: meter), (**b**) temperature (T, unit: K), (**c**) relative humidity (RH, unit: %), and (**d**) u and (**e**) v wind speed (U and V, unit: m/s), respectively.

The RMSE differences shown in Figure 8 also reveal the improvement of the model forecast through DA processes. Negative (positive) values indicate that the forecast ability of wRO is better (worse) than nRO. In general, the negative RMSE discrepancy reveals the robust improvement of the forecast performance with FS7 RO refractivity assimilation over most periods. Furthermore, the enhanced local improvement in late August and early September is related to the improvement of the typhoon track forecast, which again sheds light on the value of FS7 RO refractivity data for model forecast ability enhancement.
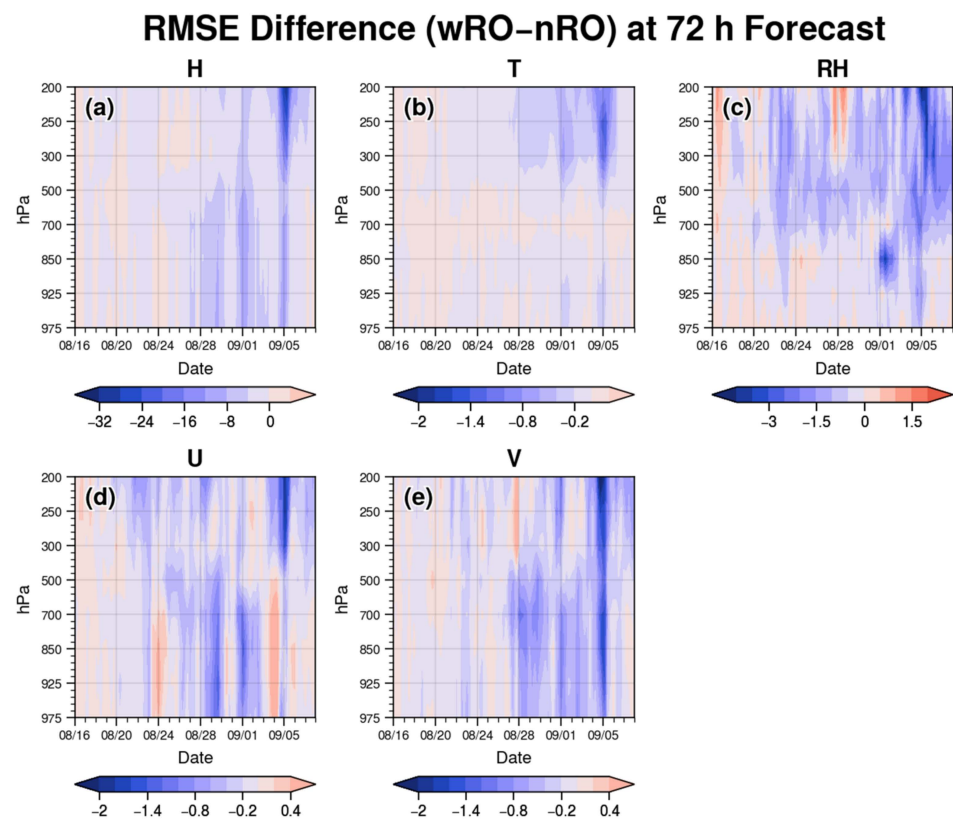
Figure 8. RMSE difference of 72-h forecast grid verification between nRO and wRO against $0.25° \times 0.25°$ NCEP GFS analysis. The vertical profiles vary with the 93 initial time during the experiment period in (**a**) geopotential height (H, unit: meter), (**b**) temperature (T, unit: K), (**c**) relative humidity (RH, unit: %), and (**d**) u and (**e**) v wind speed (U and V, unit: m/s), respectively.

4. Impact of FS7 RO Data on Typhoon Prediction

Previous studies report that the assimilation of RO observations has greatly contributed to tropical cyclone genesis [16,17] and track and intensity prediction [10,18–23]. As mentioned, there have been three typhoons whose lifetimes were longer than 5 days during the experiment period. Figure 9 shows the CWB best tracks for these three typhoons, namely, Bavi, Maysak, and Haishen. The colors of the markers denote the typhoon's maximum wind speeds. However, since the total cases might be insufficient to clarify the strength of the DA effects of the FS7 RO data, another experiment was conducted, whose period was from 0000 UTC 01 October to 1800 UTC 10 October 2019, corresponding to Typhoon Hagibis, whose track is also shown in Figure 9. For this typhoon case, the DA cycles were also four times per day at 00/06/12/18 UTC, as in the prior experiment, and the initial 4 days were designed for model spin-up. Typhoon Hagibis is a case with a long lifetime, and its maximum center wind speed had exceeded 51 m/s and persisted for more than 3 days.

4.1. Typhoon Track and Intensity

The following statistics of typhoons were composed of four typhoons and evaluated over 70 forecasts in all experiment periods. Figure 10 illustrates the statistics of mean typhoon track errors, intensity errors, and corresponding total forecast cases. In track errors (Figure 10a), assimilating FS7 RO data can improve prediction within the first 2 days, as demonstrated by the 95% confidence intervals of the experiment differences. At the same time, the minimum central pressure was selected as the typhoon intensity criterion. Figure 10b shows the mean absolute error differences between the best track minimum center pressure and that of wRO/nRO. Regarding the 95% confidence intervals of the

differences, although all the intensities simulated by the model were weaker than the best track (since the values are positive), FS7 RO DA reduces intensity errors at almost all forecast hours. However, the pressure differences in the initial condition were around 30 hPa even assimilating with FS7 RO data. An improved typhoon initialization process and increased model horizontal resolution can further mitigate the deficiency of the intensity prediction.
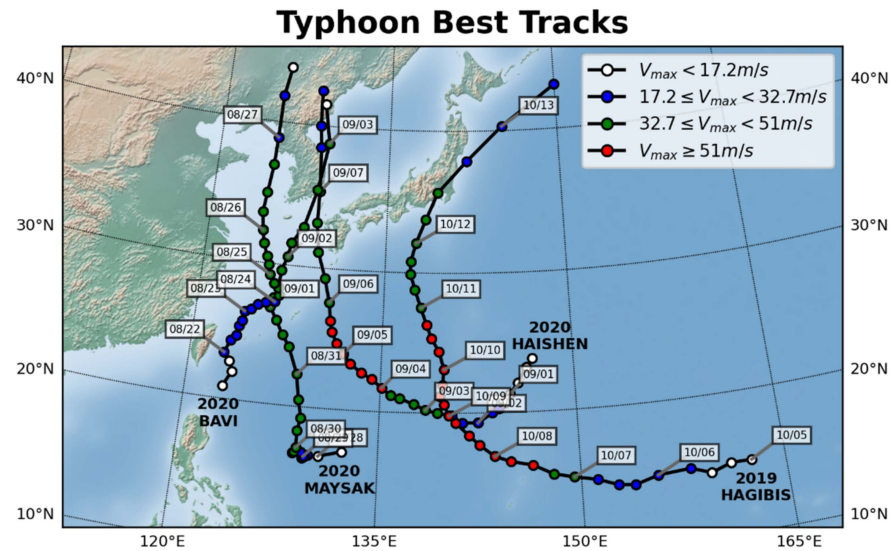

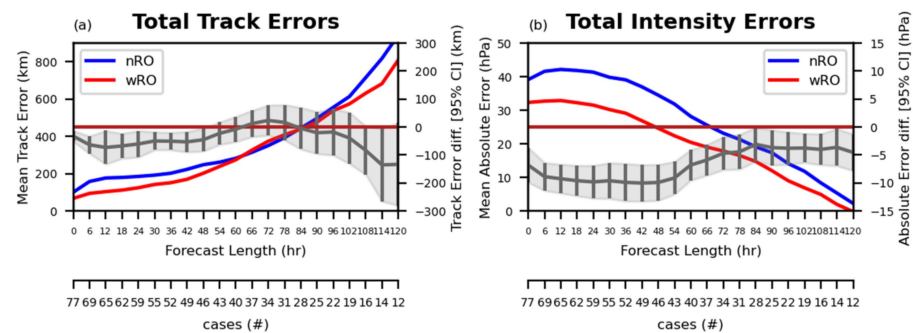**Figure 9.** Best tracks of Typhoon Hagibis (2019), Bavi (2020), Maysak (2020), and Haishen (2020).

Figure 10. (**a**) Average typhoon track errors and (**b**) intensity errors for four typhoons, namely, Bavi, Maysak, Haishen, and Hagibis. The nRO and wRO are shown in blue and red, respectively, and their differences with 95% confidence intervals are shown in gray. The numbers of forecast cases are printed at the lowest axis.

4.2. Typhoon Structure

The full-cycle DA strategy was utilized in this study. In spite of the first cycle, the first guess of the full cyclic DA, also called "background", was from the 6-h forecast of the previous run. Therefore, the previous cycles' observations have influenced the skill of this short forecast allowing their impact to accumulate over time in the cycling DA.

Figure 11 depicts the initial condition of Typhoon Haishen at 0000 UTC on 3 September 2020. As shown in Figure 11a, at this time, Typhoon Haishen has developed a robust typhoon structure, and the maximum wind speed can reach 32.7 m/s. In the nRO experiment (Figure 11b), almost no typhoon circulation was observed in the initial field; however, in the wRO experiment (Figure 11c), a more obvious cyclonic circulation was noted, and the position of the model typhoon is quite close to the observation. This improvement could be the result of increasing the moisture field over the open ocean from assimilating FS7 RO data, as shown in Figure 5. In particular, the robust RO impact in the wRO experiment is partly due to the accumulation of the observation effect and partly from the reduced spin-up effect in the full cyclic DA. This result is consistent with previous studies [16,17].
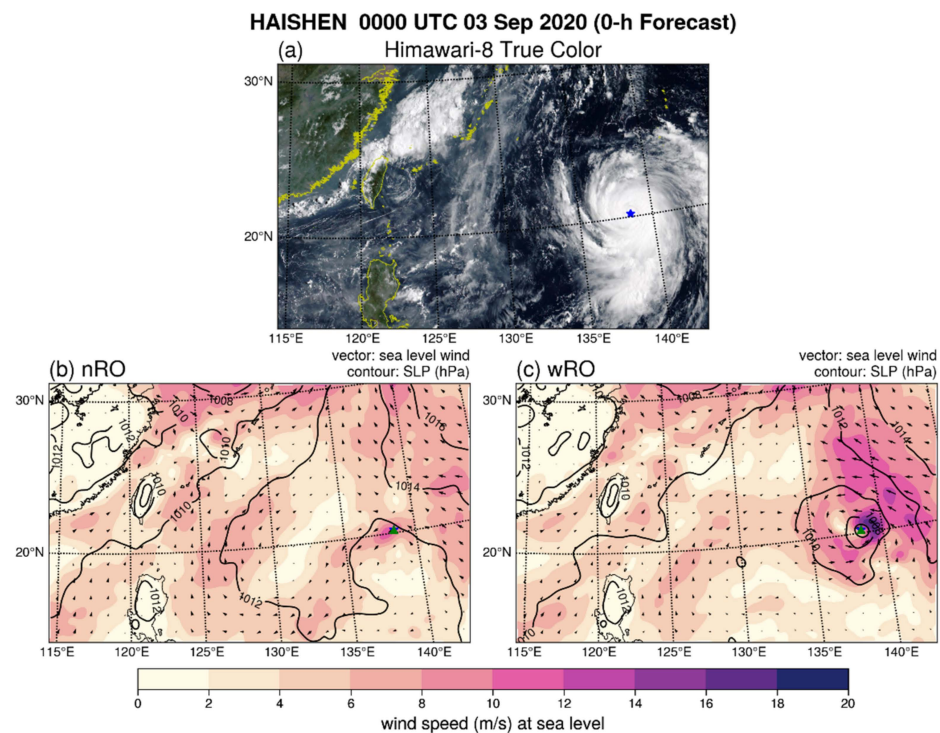
Figure 11. (**a**) True color image from Himawari-8, (**b**) the initial condition within nRO and (**c**) wRO of Typhoon Haishen at 0000 UTC on 03 September 2020. The green stars denote the central positions of the best track at this time.

Figure 12 shows the model results for Typhoon Haishen at 1800 UTC on 3 September 2020 for the analysis field and the forecast at lead times of 96, 72, 48, and 24 h, respectively. Satellite observations at the same time are similar to those in Figure 11a. The figure shows that in the nRO experiment, the model forecast of different lead times could not produce the circulation of the typhoon. For the wRO experiment, the typhoon structure was more robust, increasing with lead times, and the forecast track error remained limited. It implies that the improved initial typhoon structure, as shown in Figure 11, results in a better model prediction both in typhoon position and structure. The results can explain the reason why the wRO experiment shown in Figure 10b improves the typhoon intensity forecast results.
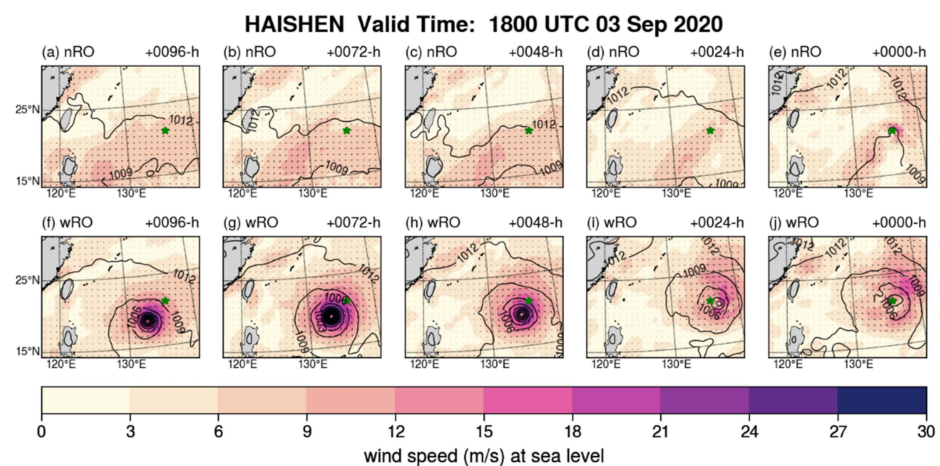

Figure 12. Typhoon Haishen initial conditions of lead times from 96 to 00 h within (**a**–**e**) nRO and (**f**–**j**) wRO validated at 1800 UTC on 3 September 2020. The green star signs denote the central positions of the best track, where the central pressure is 940 hPa and the maximum wind speed is 45 m/s at this time.

5. Conclusions

FORMOSAT-7/COSMIC-2 (FS7/C2) was successfully launched on 25 June 2019 and provided at least 4000 RO soundings per day covering the tropics to the subtropics. As the successor of FORMOSAT-3/COSMIC (FS3/C1), FS7 not only provides high-quality profile data, but most of its data can even penetrate into the lower atmosphere, exceeding the FS3 observation limit. This study aimed to evaluate the impact of assimilating FS7 RO data on a regional model, especially in the operational NWP system of the CWB, from the perspectives of the synoptic and high-impact weather systems. In this study, the operational CWBWRF numerical model with the 3DEnVar data assimilating system was adapted, but only the largest domain with 15-km model grid spacing was utilized. The following two experiments were conducted: one assimilated Global Telecommunication System in-situ observations as in the CWB operational task (nRO), and the other additionally assimilated FS7 RO refractivity profiles (wRO). Both experiments utilized 6-h assimilating window and full cycle DA strategy from 1200 UTC 05 August to 1200 UTC 07 September 2020 and made 120-h forecasts after each assimilation. In the experiment period, three typhoons, namely, Bavi, Maysak, and Haishen, were generated in the model domain and persisted over 3 days, adding large uncertainty to the forecast results.

First, the RO refractivity profile usage in the assimilating process was investigated. Data rejection rates increased dramatically from 6 km to near the surface. Although the FS7 signal can penetrate down to near the surface, most of the low-level refractive profiles were not assimilated due to the current strict QC criteria in CWBWRF DA. The error statistics of OmB and OmA showed that the QC procedure filtered bad data effectively. Although the model only assimilated a small amount of low-level FS7 RO data, it was still able to correct the variables at lower levels through the vertical error correlation (BEC). The analysis increment differences (wRO-nRO) represent the impact of RO observation on the analysis. The results show that FS7 RO data could suppress the temperature increases at the model's upper levels and correct model dry bias features effectively by adding more moisture across the model domain.

Second, averaging the 93 cases of 0-h, 72-h, and 120-h forecasts, both the domain-averaged forecast ME and RMSE were smaller in the wRO experiments. The biases of geopotential height, temperature, and wind were reduced above 500 hPa, while for RH, the improvement was between 750 and 250 hPa. In addition, the RMSE showed that FS7 RO refractivity assimilation improved model forecast ability for at least 3 days. The time series for the domain-averaged ME and RMSE of the 72-h forecast show that the model biases were mitigated and that the RMSE was reduced in the wRO experiment through the experimental period. This result sheds light on the value of FS7 RO DA for modeling synoptic prediction.

Typhoon prediction is another topic of focus. In this study, cases of four typhoons, namely, Hagibis, Bavi, Maysak, and Haishen, provided 70 forecasts to evaluate the RO impact on the typhoon forecast. In track errors, assimilating FS7 RO data significantly improved predictability in the leading 2 days. Meanwhile, although all the typhoon intensities were weaker than the best track, FS7 RO DA could alleviate this deficiency, and all the intensity forecasts were improved. However, the intensities of all simulated typhoons were insufficient even after assimilating FS7 RO data. The deficiency of the intensity prediction could be further mitigated by improving the typhoon initialization process and increasing the model's horizontal resolution.

In the case study of Typhoon Haishen, compared with the nRO experiment, the assimilation of RO observation developed a robust typhoon structure in the initial condition, and the better initial condition further improved the typhoon structure prediction at different lead times of 96, 72, 48, and 24-h, respectively. Improving the dry bias by assimilating the RO observation could be an important factor in improving the typhoon structure analysis and prediction.

This study has demonstrated that FS7 RO DA significantly benefited model prediction. These impressive results have led to the operational use of the FS7 RO data in the CWB

deterministic regional model since 28 May 2021. However, it should be noted that the default FS7 RO QC procedure in CWBWRF would eliminate most low-level RO profiles. Although model first guesses could be corrected by BEC in DA and could lead to a positive impact on the forecast performance, the good signal penetration of FS7 was wasted. To better use the low-level FS7 RO data, the dedicated QC procedure should be further investigated in advance of usage.

References

1. Anthes, R.A.; Rocken, C.; Kuo, Y.-H. Applications of COSMIC to Meteorology and Climate. *Terr. Atmospheric Ocean. Sci.* **2000**, *11*, 115–156. [CrossRef]
2. Kursinski, E.R.; Hajj, G.A.; Schofield, J.T.; Linfield, R.P.; Hardy, K.R. Observing Earth's atmosphere with radio occultation measurements using the Global Positioning System. *J. Geophys. Res. Atmos.* **1997**, *102*, 23429–23465. [CrossRef]
3. Kursinski, E.R.; Hajj, G.A.; Leroy, S.S.; Herman, B. The GPS Radio Occultation Technique. *Terr. Atmos. Ocean. Sci.* **2000**, *11*, 053. [CrossRef]
4. Wickert, J.; Reigber, C.; Beyerle, G.; König, R.; Marquardt, C.; Schmidt, T.; Grunwaldt, L.; Galas, R.; Meehan, T.K.; Melbourne, W.G.; et al. Atmosphere sounding by GPS radio occultation: First results from CHAMP. *Geophys. Res. Lett.* **2001**, *28*, 3263–3266. [CrossRef]
5. Healy, S.B.; Thépaut, J.-N. Assimilation experiments with CHAMP GPS radio occultation measurements. *Q. J. R. Meteorol. Soc.* **2006**, *132*, 605–623. [CrossRef]
6. Hajj, G.A.; Ao, C.O.; Iijima, B.A.; Kuang, D.; Kursinski, E.R.; Mannucci, A.J.; Meehan, T.K.; Romans, L.J.; de la Torre Juarez, M.; Yunck, T.P. CHAMP and SAC-C atmospheric occultation results and intercomparisons. *J. Geophys. Res. Atmos.* **2004**, *109*, D06109. [CrossRef]
7. Tapley, B.D.; Bettadpur, S.; Ries, J.C.; Thompson, P.F.; Watkins, M.M. GRACE Measurements of Mass Variability in the Earth System. *Science* **2004**, *305*, 503–505. [CrossRef]
8. Luntama, J.-P.; Kirchengast, G.; Borsche, M.; Foelsche, U.; Steiner, A.; Healy, S.; Von Engeln, A.; O'Clerigh, E.; Marquardt, C. Prospects of the EPS GRAS Mission For Operational Atmospheric Applications. *Bull. Am. Meteorol. Soc.* **2008**, *89*, 1863–1876. [CrossRef]
9. Lee, S.-R. Overview of KOMPSAT-5 program, mission, and system. In Proceedings of the IEEE International Geoscience and Remote Sensing Symposium, Honolulu, HI, USA, 25–30 July 2010; pp. 797–800. [CrossRef]
10. Hsiao, L.-F.; Chen, D.-S.; Kuo, Y.-H.; Guo, Y.-R.; Yeh, T.-C.; Hong, J.-S.; Fong, C.-T.; Lee, C.-S. Application of WRF 3DVAR to Operational Typhoon Prediction in Taiwan: Impact of Outer Loop and Partial Cycling Approaches. *Weather Forecast.* **2012**, *27*, 1249–1263. [CrossRef]
11. Cucurull, L.; Anthes, R.A.; Tsao, L.-L. Radio Occultation Observations as Anchor Observations in Numerical Weather Prediction Models and Associated Reduction of Bias Corrections in Microwave and Infrared Satellite Observations. *J. Atmospheric Ocean. Technol.* **2014**, *31*, 20–32. [CrossRef]

12. Kuo, Y.-H.; Wee, T.-K.; Sokolovskiy, S.; Rocken, C.; Schreiner, W.; Hunt, D.; Anthes, R. Inversion and Error Estimation of GPS Radio Occultation Data. *J. Meteorol. Soc. Jpn. Ser. II* **2004**, *82*, 507–531. [CrossRef]

13. Ho, S.-P.; Anthes, R.A.; Ao, C.O.; Healy, S.; Horanyi, A.; Hunt, D.; Mannucci, A.J.; Pedatella, N.; Randel, W.J.; Simmons, A.; et al. The COSMIC/FORMOSAT-3 Radio Occultation Mission after 12 Years: Accomplishments, Remaining Challenges, and Potential Impacts of COSMIC-2. *Bull. Am. Meteorol. Soc.* **2020**, *101*, E1107–E1136. [CrossRef]

14. Chien, F.-C.; Hong, J.-S.; Kuo, Y.-H. Estimation of Marine Boundary Layer Heights over the Western North Pacific Using GPS Radio Occultation Profiles. *SOLA* **2016**, *12*, 302–306. [CrossRef]

15. Chien, F.-C.; Hong, J.-S.; Kuo, Y.-H. The Marine Boundary Layer Height over the Western North Pacific Based on GPS Radio Occultation, Island Soundings, and Numerical Models. *Sensors* **2019**, *19*, 155. [CrossRef]

16. Chen, S.-Y.; Wee, T.-K.; Kuo, Y.-H.; Bromwich, D.H. An Impact Assessment of GPS Radio Occultation Data on Prediction of a Rapidly Developing Cyclone over the Southern Ocean. *Mon. Weather Rev.* **2014**, *142*, 4187–4206. [CrossRef]

17. Chen, S.-Y.; Kuo, Y.-H.; Huang, C.-Y. The Impact of GPS RO Data on the Prediction of Tropical Cyclogenesis Using a Nonlocal Observation Operator: An Initial Assessment. *Mon. Weather Rev.* **2020**, *148*, 2701–2717. [CrossRef]

18. Chen, S.-Y.; Huang, C.-Y.; Kuo, Y.-H.; Guo, Y.-R.; Shiau, S. Assimilation of GPS Refractivity from FORMOSAT-3/COSMIC Using a Nonlocal Operator with WRF 3DVAR and Its Impact on the Prediction of a Typhoon Event. *Terr. Atmospheric Ocean. Sci.* **2009**, *20*, 133. [CrossRef]

19. Chen, S.-Y.; Shih, C.-P.; Huang, C.-Y.; Teng, W.-H. An Impact Study of GNSS RO Data on the Prediction of Typhoon Nepartak (2016) Using a Multi-resolution Global Model with 3D-Hybrid Data Assimilation. *Weather Forecast.* **2021**, *36*, 957–977. [CrossRef]

20. Kuo, Y.-H.; Liu, H.; Guo, Y.-R.; Terng, C.-T.; Lin, Y.-T. Impact of FORMOSAT-3/COSMIC Data on Typhoon and Meiyu Prediction. In *Recent Progress in Atmospheric Sciences: Impact of FORMOSAT-3/COSMIC Data on Typhoon and Meiyu Prediction: Application to the Asia-Pacific Region*; World Scientific: Singapore, 2008; pp. 458–483. [CrossRef]

21. Chen, Y.-C.; Hsieh, M.-E.; Hsiao, L.-F.; Kuo, Y.-H.; Yang, M.-J.; Huang, C.-Y.; Lee, C.-S. Systematic evaluation of the impacts of GPSRO data on the prediction of typhoons over the northwestern Pacific in 2008–2010. *Atmos. Meas. Tech.* **2015**, *8*, 2531–2542. [CrossRef]

22. Huang, C.-Y.; Kuo, Y.-H.; Chen, S.-H.; Vandenberghe, F. Improvements in Typhoon Forecasts with Assimilated GPS Occultation Refractivity. *Weather Forecast.* **2005**, *20*, 931–953. [CrossRef]

23. Huang, C.-Y.; Kuo, Y.-H.; Chen, S.-Y.; Terng, C.-T.; Chien, F.-C.; Lin, P.-L.; Kueh, M.-T.; Yang, M.-J.; Wang, C.-J.; Rao, A.S.K.A.V.P. Impact of GPS radio occultation data assimilation on regional weather predictions. *GPS Solut.* **2009**, *14*, 35–49. [CrossRef]

24. Yang, S.-C.; Chen, S.-H.; Huang, C.-Y.; Chen, C.-S. Evaluating the Impact of the COSMIC RO Bending Angle Data on Predicting the Heavy Precipitation Episode on 16 June 2008 during SoWMEX-IOP8. *Mon. Weather Rev.* **2014**, *142*, 4139–4163. [CrossRef]

25. Huang, C.-Y.; Chen, S.-Y.; Anisetty, S.K.A.V.P.R.; Yang, S.-C.; Hsiao, L.-F. An Impact Study of GPS Radio Occultation Observations on Frontal Rainfall Prediction with a Local Bending Angle Operator. *Weather Forecast.* **2016**, *31*, 129–150. [CrossRef]

26. Tu, C.-C.; Chen, Y.-L.; Chen, S.-Y.; Kuo, Y.-H.; Lin, P.-L. Impacts of Including Rain-Evaporative Cooling in the Initial Conditions on the Prediction of a Coastal Heavy Rainfall Event during TiMREX. *Mon. Weather Rev.* **2017**, *145*, 253–277. [CrossRef]

27. Schreiner, W.S.; Weiss, J.P.; Anthes, R.A.; Braun, J.; Chu, V.; Fong, J.; Hunt, D.; Kuo, Y.-H.; Meehan, T.; Serafino, W.; et al. COSMIC-2 Radio Occultation Constellation: First Results. *Geophys. Res. Lett.* **2020**, *47*, e2019GL086841. [CrossRef]

28. Ruston, B.; Healy, S. Forecast Impact of FORMOSAT -7/ COSMIC -2 GNSS Radio Occultation Measurements. *Atmospheric Sci. Lett.* **2020**, *22*, e1019. [CrossRef]

29. Lien, G.-Y.; Lin, C.-H.; Huang, Z.-M.; Teng, W.-H.; Chen, J.-H.; Lin, C.-J.; Ho, H.-H.; Huang, J.-Y.; Hong, J.-S.; Cheng, C.-P.; et al. Assimilation Impact of Early FORMOSAT-7/COSMIC-2 GNSS Radio Occultation Data with Taiwan's CWB Global Forecast System. *Mon. Weather Rev.* **2021**, *149*, 2171–2191. [CrossRef]

30. Ho, S.-P.; Zhou, X.; Shao, X.; Zhang, B.; Adhikari, L.; Kireev, S.; He, Y.; Yoe, J.; Xia-Serafino, W.; Lynch, E. Initial Assessment of the COSMIC-2/FORMOSAT-7 Neutral Atmosphere Data Quality in NESDIS/STAR Using In Situ and Satellite Data. *Remote Sens.* **2020**, *12*, 4099. [CrossRef]

31. Chen, S.-Y.; Liu, C.-Y.; Huang, C.-Y.; Hsu, S.-C.; Li, H.-W.; Lin, P.-H.; Cheng, J.-P.; Huang, C.-Y. An Analysis Study of FORMOSAT-7/COSMIC-2 Radio Occultation Data in the Troposphere. *Remote Sens.* **2021**, *13*, 717. [CrossRef]

32. Healy, S. ECMWF starts assimilating COSMIC-2 data. *ECMWF Newsl.* **2020**, *163*, 5–6. Available online: https://www.ecmwf.int/sites/default/files/elibrary/2020/19508-newsletter-no-163-spring-2020.pdf (accessed on 4 May 2022).

33. Shao, H.; Bathmann, K.; Zhang, H.; Huang, Z.-M.; Cucurull, L.; Vandenberghe, F.; Treadon, R.; Kleist, D.; Yoe, J.G. COS-MIC-2 NWP Assessment and Implementation at JCSDA and NCEP. In Proceedings of the 5th International Conference on GPS Radio and Occultation, Taipei, Taiwan, 27–29 May 2020.

34. Anthes, R.; Sjoberg, J.; Rieckh, T.; Wee, T.-K.; Zeng, Z. COSMIC-2 radio occultation temperature, specific humidity, and precipitable water in Hurricane Dorian (2019). *Terr. Atmos. Ocean. Sci.* **2021**, *32*, 925–938. [CrossRef]

35. Singh, R.; Ojha, S.P.; Anthes, R.; Hunt, D. Evaluation and Assimilation of the COSMIC-2 Radio Occultation Constellation Observed Atmospheric Refractivity in the WRF Data Assimilation System. *J. Geophys. Res. Atmos.* **2021**, *126*, e2021JD034935. [CrossRef]

36. Chen, Y.-C.; Tsai, C.-C.; Wu, Y.-C.; Wang, A.-H.; Wang, C.-J.; Lin, H.-H.; Chen, D.-R.; Yu, Y.-C. Evaluation of Operational Monsoon Moisture Surveillance and Severe Weather Prediction Utilizing COSMIC-2/FORMOSAT-7 Radio Occultation Observations. *Remote Sens.* **2021**, *13*, 2979. [CrossRef]

37. Chen, S.-Y.; Nguyen, T.-C.; Huang, C.-Y. Impact of Radio Occultation Data on the Prediction of Typhoon Haishen (2020) with WRFDA Hybrid Assimilation. *Atmosphere* **2021**, *12*, 1397. [CrossRef]

38. Chang, C.-C.; Yang, S.-C. Impact of assimilating Formosat-7/COSMIC-II GNSS radio occultation data on heavy rainfall prediction in Taiwan. *Terr. Atmos. Ocean. Sci.* **2022**, *33*, 7. [CrossRef]

39. Liou, C.; Chen, J.; Terng, C.; Wang, F.; Fong, C.; Rosmond, T.E.; Kuo, H.; Shiao, C.; Cheng, M. The Second–Generation Global Forecast System at the Central Weather Bureau in Taiwan. *Weather Forecast.* **1997**, *12*, 653–663. [CrossRef]

40. Skamarock, W.C.; Klemp, J.B.; Dudhia, J.; Gil, D.A.; Barker, D.M.; Duda, M.G.; Huang, X.Y.; Wang, W.; Powers, J.G. *Description of the Advanced Research WRF Version 3*; National Center for Atmospheric Research: Boulder, CO, USA, 2008.

41. Hong, S.-Y.; Noh, Y.; Dudhia, J. A New Vertical Diffusion Package with an Explicit Treatment of Entrainment Processes. *Mon. Weather Rev.* **2006**, *134*, 2318–2341. [CrossRef]

42. Tao, W.-K.; Wu, D.; Lang, S.; Chern, J.-D.; Peters-Lidard, C.; Fridlind, A.; Matsui, T. High-resolution NU-WRF simulations of a deep convective-precipitation system during MC3E: Further improvements and comparisons between Goddard microphysics schemes and observations. *J. Geophys. Res. Atmos.* **2016**, *121*, 1278–1305. [CrossRef]

43. Iacono, M.J.; Delamere, J.S.; Mlawer, E.J.; Shephard, M.W.; Clough, S.A.; Collins, W.D. Radiative forcing by long-lived greenhouse gases: Calculations with the AER radiative transfer models. *J. Geophys. Res. Atmos.* **2008**, *113*, D13103. [CrossRef]

44. Tewari Chen, F.; Wang, W.; Dudhia, J.; LeMone, M.A.; Mitchell, K.; Ek, M.; Gayno, G.; Wegiel, J.; Cuenca, R.H. 2004: Implementation and Verification of the Unified Noah Land Surface Model in the WRF Model. In Proceedings of the Joint between the Symposium on Forecasting the Weather and Climate of the Atmosphere and Ocean and the 20th Conference on Weather Analysis and Forecasting/16th Conference on Numerical Weather Prediction, Seattle, WA, USA, 12–15 January 2004. Available online: https://ams.confex.com/ams/pdfpapers/69061.pdf (accessed on 7 July 2022).

45. Cucurull, L.; Derber, J.C.; Treadon, R.; Purser, R.J. Assimilation of Global Positioning System Radio Occultation Observations into NCEP's Global Data Assimilation System. *Mon. Weather Rev.* **2007**, *135*, 3174–3193. [CrossRef]

46. Cucurull, L.; Derber, J.C.; Purser, R.J. A bending angle forward operator for global positioning system radio occultation measurements. *J. Geophys. Res. Atmos.* **2013**, *118*, 14–28. [CrossRef]

47. Cucurull, L.; Atlas, R.; Li, R.; Mueller, M.J.; Hoffman, R.N. An Observing System Simulation Experiment with a Constellation of Radio Occultation Satellites. *Mon. Weather Rev.* **2018**, *146*, 4247–4259. [CrossRef]

48. Poli, P.; Healy, S.B.; Dee, D.P. Assimilation of Global Positioning System radio occultation data in the ECMWF ERA-Interim reanalysis. *Q. J. R. Meteorol. Soc.* **2010**, *136*, 1972–1990. [CrossRef]

49. Poli, P.; Moll, P.; Puech, D.; Rabier, F.; Healy, S.B. Quality Control, Error Analysis, and Impact Assessment of FORMOSAT-3/COSMIC in Numerical Weather Prediction. *Terr. Atmos. Ocean. Sci.* **2009**, *20*, 101. [CrossRef]

50. Cucurull, L. Implementation of a quality control for radio occultation observations in the presence of large gradients of atmospheric refractivity. *Atmos. Meas. Tech.* **2015**, *8*, 1275–1285. [CrossRef]

51. Cucurull, L. Improvement in the Use of an Operational Constellation of GPS Radio Occultation Receivers in Weather Forecasting. *Weather Forecast.* **2010**, *25*, 749–767. [CrossRef]